

Genesis locations of the costliest atmospheric rivers impacting the Western United States

Hamish D Prince¹, Peter B Gibson¹, Michael J DeFlorio², Thomas Corringham², Alison Cobb³, Bin Guan⁴, F. Martin Ralph⁵, and Duane Edward Waliser⁶

¹Center for Western Weather and Water Extremes, Scripps Institution of Oceanography, University of California, San Diego

²Scripps Institution of Oceanography

³University of California, San Diego

⁴UCLA

⁵SIO

⁶Jet Propulsion Laboratory

November 24, 2022

Abstract

Atmospheric rivers (ARs) are responsible for the vast majority (approximately 88%) of flood damage in the Western U.S, an annual average of USD\$1.1 billion. Here, using historical flood insurance data, we investigate the genesis characteristics of damaging ARs in the Western U.S. ARs exceeding USD\$20 million in damage (90th percentile), are shown to travel further across the Pacific Ocean, with median genesis locations 8° to 27° longitude further westward compared to typical ARs. Identifying regions of preferential genesis of damaging ARs elicit important implications for AR observation campaigns, highlighting distant regions not currently considered for AR reconnaissance. The genesis of damaging ARs is associated with elevated upper-level zonal wind speeds along with deeper cyclonic anomalies, most pronounced for Washington and Oregon ARs. Linking AR dynamics and lifecycle characteristics to economic damage provides an opportunity for impact-based forecasting of ARs prior to landfall, supporting efforts to mitigate extreme flood damages.

1 **Genesis locations of the costliest atmospheric rivers impacting the Western**
2 **United States**

3 **Hamish D. Prince^{1*}, Peter B. Gibson¹, Michael J. DeFlorio¹, Thomas W, Corringham¹,**
4 **Alison Cobb¹, Bin Guan^{2,3}, F. Martin Ralph¹ and Duane E. Waliser^{2,3}**

5 ¹Center for Western Weather and Water Extremes, Scripps Institution of Oceanography, University of
6 California, San Diego, La Jolla, CA, USA,

7 ²Jet Propulsion Laboratory, California Institute of Technology, Pasadena, CA, USA,

8 ³Joint Institute for Regional Earth System Science and Engineering, University of California, Los
9 Angeles, CA, USA

10 **Corresponding author: Hamish Prince, prince.hamishd@gmail.com*

11 **Key Points:**

- 12 • Historical flood damages from the Western U.S. are paired with an atmospheric river
13 lifecycle tracking algorithm
- 14 • Damaging atmospheric rivers tend to have genesis locations further from the coastline,
15 travel further and have a higher moisture flux
- 16 • The genesis of damaging atmospheric rivers is associated with distinct dipole pressure
17 anomalies paired with an elevated zonal jet stream

18 **Word count (including figure captions): 3,974**

19 **Word limit:4,000**

20 **Four Figures**

21 **Abstract**

22 Atmospheric rivers (ARs) are responsible for the vast majority (approximately 88%) of flood damage
23 in the Western U.S, an annual average of USD\$1.1 billion. Here, using historical flood insurance data,
24 we investigate the genesis characteristics of damaging ARs in the Western U.S. ARs exceeding USD\$20
25 million in damage (90th percentile), are shown to travel further across the Pacific Ocean, with median
26 genesis locations 8° to 27° longitude further westward compared to typical ARs. Identifying regions of
27 preferential genesis of damaging ARs elicit important implications for AR observation campaigns,
28 highlighting distant regions not currently considered for AR reconnaissance. The genesis of damaging
29 ARs is associated with elevated upper-level zonal wind speeds along with deeper cyclonic anomalies,
30 most pronounced for Washington and Oregon ARs. Linking AR dynamics and lifecycle characteristics
31 to economic damage provides an opportunity for impact-based forecasting of ARs prior to landfall,
32 supporting efforts to mitigate extreme flood damages.

33 **Plain Language Summary**

34 We examine the economic impact of atmospheric rivers, corridors or elevated atmospheric moisture
35 vapor transport, on the Western U.S. Atmospheric rivers are responsible for the vast majority of flood
36 damage which is experienced in the Western U.S. causing mean annual damages of USD\$1.1 billion,
37 88% of the total annual flood damage. We use 40 years of historic flood insurance claims paired with a
38 database of all atmospheric rivers that make landfall on the U.S. West Coast to show, for the first time,
39 the relationship between atmospheric river dynamics and the economic impact for the Western. U.S.
40 Our results show that damaging atmospheric rivers tend to originate further from the U.S. coastline than
41 all other, less damaging atmospheric rivers. We also demonstrate the atmospheric conditions favourable
42 for the initiation of damaging atmospheric rivers with a particular focus on atmospheric rivers that travel
43 across the entire Pacific Ocean prior to landfall. Clear implications arise for AR data collection,
44 identifying important regions which are not current examined where damaging ARs generate. The
45 results presented aid in understanding the cause of damaging floods in the Western U.S. with the aim
46 of supporting atmospheric river forecasts by linking atmospheric conditions to historic damage.

47 **1. Introduction**

48 Atmospheric rivers (ARs) are filamentary corridors of enhanced atmospheric water vapor transport that
49 can produce extreme precipitation in mid-latitude regions, particularly when an AR undergoes ascent
50 through interaction with topography (Zhu and Newell, 1998; Neiman et al., 2008). The magnitude and
51 duration of the moisture flux directly relates to the intensity of precipitation with the highest
52 precipitation rates being associated with strong, prolonged ARs (Konrad and Dettinger, 2017; Ralph et
53 al., 2019; Eiras-Barca et al., 2021; Prince et al., 2021). Given the association between ARs and
54 precipitation, the occurrence of ARs brings the potential for substantial environmental and
55 socioeconomic impacts (Corringham et al., 2019). On the West Coast of the U.S., landfalling ARs are
56 the primary cause of flooding with approximately 90% of all floods occurring during ARs (Dettinger et
57 al., 2011; Paltan et al., 2017). The occurrence of these hydrological extremes often results in damage to
58 property and infrastructure, a noteworthy event being the damage to the Oroville Dam in northern
59 California resulting in mass evacuations and financial damages exceeding USD\$1 billion (Vano et al.,
60 2019; White et al., 2019). A primary mitigation of AR damage in the Northeast Pacific are operational
61 reconnaissance campaigns, sampling ARs that impact the U.S. West Coast to improve forecasts of
62 extreme precipitation (e.g. AR Recon, Ralph et al., 2020; Stone et al. 2020). AR Recon targets ARs at
63 1-5 days lead time (primarily between 180°W and the U.S. West Coast) and understanding the lifecycle
64 (genesis and progression) and damage of ARs is important for identifying and sampling impactful ARs.

65 *1.1 Atmospheric river damages*

66 The financial cost of ARs in the Western U.S. was quantitatively examined by Corringham et al. (2019),
67 demonstrating that over 84% of all flood losses are associated with ARs, exceeding 95% in coastal
68 locations. The most extreme individual ARs are shown to exceed USD\$3 billion in flood damages, with
69 13 ARs exceeding USD\$1 billion over a 40-year period (Corringham et al., 2019). Furthermore, the
70 majority of AR damage is shown to be attributed to a very small number of intense ARs with a distinct
71 relationship between the magnitude and duration of AR and the experienced damage (Corringham et
72 al., 2019). The financial cost of ARs has also been assessed in Europe, where ARs were found to account
73 for 75% of the high-impact wind storms during 1997-2013, with extreme events exceeding USD\$2
74 billion in damages in some cases (Waliser and Guan, 2017).

75 *1.2 Atmospheric river lifecycle tracking*

76 Rutz et al. (2020) highlights the importance of considering ARs through a Lagrangian perspective to
77 understand their life cycle dynamics, specifying that automatic tracking of ARs in time and space has
78 previously been a challenging endeavour. Recent advances in AR detection techniques (ARDTs) have
79 allowed for the identification of full life cycle characteristics of ARs including the genesis location,

80 termination location, relative age, merging and separation (Zhou et al. 2018; Guan and Waliser, 2019;
81 Zhou and Kim, 2019; Shearer et al. 2020). The study of AR life cycles remains as a key research gap
82 identified as part of the AR Tracking Method Intercomparison Project (ARTMIP), a coordinated effort
83 to quantify uncertainties in AR tracking and consequent conclusions (Shields et al., 2018; Rutz et al.
84 2019; O’Brian et al., 2020). Zhou and Kim (2019) have previously examined the impact and dynamics
85 of AR genesis associated with the U.S. West Coast, finding that ARs with genesis locations in the
86 Western Pacific (west of 170°W) tend to bring more rain to northern locations while Eastern Pacific
87 ARs tend to bring rain to southern locations on the U.S. West Coast. Furthermore, it was also identified
88 that ARs that travel further, from the Western Pacific, tend to have a higher IVT than ARs travelling
89 from the Eastern Pacific (an approximate 30% increase) and last for longer (an average of approximately
90 2 days more; Payne and Magnusdottir, 2014; Zhou et al., 2018; Zhou and Kim, 2019).

91 This study provides crucial impact-based insight into the importance of AR genesis in the North Pacific
92 basin through examining the relationship between genesis location and economic damage in the
93 Western U.S. To do so, a lifecycle AR database is combined with estimates of daily economic damages.
94 The synoptic-scale conditions during initiation of all ARs the most damaging ARs are also analyzed to
95 probe the dynamics associated with these devastating events.

962. **Data and methods**

97 In this study, a database of daily AR occurrence along the U.S. West Coast is developed from the Guan
98 and Waliser (2019) Version 3, Tracking Atmospheric Rivers Globally as Elongated Targets (tARget)
99 algorithm (henceforth GW₁₉). The AR catalogue used herein was obtained by extracting unique AR ID
100 values generated within GW₁₉ which are consistent throughout an entire AR lifecycle. The GW₁₉
101 catalogue was developed for the period between 1979 and 2019 (40 years) using 6-hourly instantaneous
102 fields of global integrated vapor transport (IVT) at 1.5° resolution (the specified resolution of GW₁₉)
103 from the ERA-Interim reanalysis (Dee et al., 2011). GW₁₉ applies a series of magnitude and geometric
104 threshold tests to identify elongated regions of elevated IVT. ARs at genesis are selected as the detected
105 AR objects which do not have congruent or co-located ARs in the previous timestep, effectively the
106 point in time when a region of IVT has become sufficiently large and intense to meet the geometric and
107 magnitude thresholds for AR detection. The algorithm was first presented as a spatial feature
108 identification technique (Guan and Waliser, 2015) and has since been evaluated and validated (Guan
109 and Waliser, 2015; Guan and Waliser, 2018) and upgraded (optimized axis identification, iterative
110 testing using variable IVT percentiles and exclusion of embedded tropical cyclones) with recent
111 additions facilitating the temporal feature tracking of individual ARs, allowing for the characterisation
112 of AR lifecycles (Guan et al., 2018; Guan and Waliser, 2019).

113 Landfalling ARs are detected as AR objects that intersect the coastline of North America defined by
114 ERA-Interim at 1.5° resolution (Figure 1). The coastline is divided into 4 broad regions, Washington,
115 Oregon/Northern California, California and Baja California to account for regional heterogeneities and
116 circulation variability controlling AR propagation and landfall location as described by Guirguis et al.
117 (2018) and Zhang and Villarini (2018). Over the 40-year study period, 4436 unique AR lifecycles made
118 landfall on the U.S. West Coast. An annual mean of 36 AR events was recorded for all grid cells defining
119 the U.S. West Coast (ranging between 32 and 44 ARs per year between grid cells), comparable to
120 previously reported U.S. West Coast AR occurrence (Guan and Waliser, 2019).

121 Total estimated daily flood damages are calculated from the National Flood Insurance Program (NFIP;
122 retrieved from the U.S. Federal Emergency Management Agency 2019) for a period between April
123 1979 and March 2019, spanning the same 40 year period as the AR catalogue. Only wintertime ARs
124 (NDJFM) are analyzed and presented, aligning with the AR damage season as defined by Corringham
125 et al. (2019), and all values are adjusted for inflation to 2020 USD. The insured losses are used as a
126 proxy for total economic impact from floods based on Corringham et al. (2019) who calculated that
127 total flood damages are approximately 30 times greater than reported NFIP-insured losses; a conversion
128 used herein to report total economic damage.

129 In order to pair daily damage to AR occurrence, the 6-hourly AR catalogue is reduced to a daily
130 resolution by selecting the AR object with the greatest landfalling IVT within each day (12% of ARs
131 occurred simultaneously on the same day with higher IVT ARs along the coastline and were hence
132 removed). Following daily aggregation, 3930 individual ARs remain, 15% (598) of which were
133 excluded as spurious AR life cycles (ARs which only exist in a single time-step) to avoid possible
134 double counting (following storm detection convention; Schreck et al., 2014). The final database
135 consists of 3332 individual AR lifecycles that made landfall on the U.S. West Coast over the 40-year
136 period (mean annual occurrence of 83 per year across the entire coastline). The landfall location for
137 each AR is recorded as the location which receives the maximum onshore IVT; for example, 1367 ARs
138 were recorded to experience maximum IVT in Washington, or approximately 34 per year. Following
139 identification of AR genesis locations based on economic impact, the atmospheric dynamics associated
140 with AR genesis are assessed. Geopotential height at 500 hPa, integrated vapor transport (IVT) and the
141 300 hPa zonal wind at 1.5° resolution and 6-hourly time steps are retrieved from the ERA-Interim
142 reanalysis to observe the atmospheric conditions during genesis.

1433. **Results and Discussion**

144 The total accumulated flood damage over this period was \$51.0 billion, with ARs accounting for 86%
145 of these damages (\$44.1 billion). Annually, ARs account for an average of 88% of flood insurance
146 claims with an annual mean AR damage of \$1.1 billion. The proportion of flood damage from ARs is

147 greater nearer to the coast, with California, Nevada, Oregon, and Washington all receiving over 90% of
148 the mean annual flood damage during ARs (Figure 1). The greatest total and AR-related damages are
149 recorded in California where ARs cause an average \$657 million of flood damage annually. The
150 proximity to the coastline, adjacent topographic barriers, population density, risk of infrastructure and
151 habitation of flood plains collectively contribute to this comparatively large economic impact (Dettinger
152 et al., 2011).

153 The proportion of damage in each state broadly aligns with the landfall location (Figure 1), with the
154 majority of damage generally arising from ARs that make landfall on the adjacent coastline. The AR
155 damage recorded in each state is recorded as the damage that occurs on the day and day following an
156 AR is detected anywhere along the coastline (consistent with Corringham et al., 2019). Notably, the
157 highest proportion of AR damage in Arizona, New Mexico, Colorado and Utah arise from ARs that
158 make landfall in Baja California. Rutz and Steenburgh (2012) and Neiman et al. (2013) proposed
159 suitable explanations for extreme precipitation in the southern semiarid region of the Western U.S.,
160 describing the region of low topography between northern Baja California and the Sierra Madre
161 Occidental as a suitable corridor for inland penetration of ARs without prior orographic forcing. Some
162 anomalies exist, such as the greatest proportion of flood damage in Nevada coming from ARs that make
163 landfall in Washington. One explanation may be due to migration of landfall location over the full
164 lifecycle of the event, or from simultaneous flooding at both locations due to different weather events
165 (12% of ARs made landfall simultaneously with greater magnitude ARs and subsequently excluded
166 from analysis). The landfall location (here considered as the location of maximum IVT) does not
167 account for initial or shifting landfall locations through the progression of AR, but rather represents the
168 location where the AR would be expected to be most impactful.

1693.1 *Atmospheric river genesis location based on financial impact*

170 The genesis frequency of ARs that make landfall on the U.S. West Coast is shown in Figure 2 (separated
171 by landfall region as defined in Figure 1). The frequency is calculated as the number of times an AR
172 object has a genesis stage in each grid cell divided by the total number of ARs which make landfall for
173 each region in the U.S. West Coast. The units can be interpreted as a conditional frequency; i.e., given
174 that an AR makes landfall within each region, what is the frequency of genesis AR objects at each grid
175 cell?

176 AR genesis is more regionally constrained for southern regions, with all ARs that make landfall in Baja
177 California having genesis locations centred around 25°N, immediately over the landmass of Baja
178 California. This region has been previously identified as a key region for AR genesis with ARs
179 propagating to the northeast towards the North Atlantic Ocean, aligning with the predominant northeast
180 moisture advection (Zhang and Villarini, 2018; Guan and Waliser, 2019). When considering damaging

181 ARs (75th percentile) landfalling in Baja California, there is a westward shift offshore with reduced
182 genesis frequency over the landmass of North America and an absolute increase in genesis frequency
183 of 10% over the ocean adjacent to Baja California (statistically significant, at the 90% level from a one-
184 sided Fisher-exact test).

185 The genesis location of ARs that make landfall in California extends further westward in the Pacific
186 Ocean than Baja California ARs, with elevated genesis frequencies above 5% extending to Hawaii.
187 There is a southwest shift in damaging (75th percentile) California ARs, with statistically significant
188 absolute increases in genesis frequency up to 10% centred between Hawaii and the Californian coastline
189 (140°W). Oregon/North California and Washington both exhibit similar distributions of AR genesis,
190 with elevated genesis frequencies extending west across the entire North Pacific basin towards southern
191 Japan (140°E). AR genesis is primarily centred along 30°N with a northward curve in genesis locations
192 approaching the coastline of North America (eastward of Hawaii). Damaging ARs in these two regions
193 have increased genesis frequencies in the Central and Western Pacific basin with substantial increases
194 in AR frequency westward of 180°W. This region of elevated AR frequency is similar to the definition
195 of Western Pacific AR genesis as defined by Zhou and Kim (2019). Presented here is the first
196 documentation of AR genesis locations for the U.S. West Coast, differentiated by region and damage
197 following landfall.

198 There is a broad westward shift in AR genesis location (genesis object centroid location) as damage
199 percentile increases for all regions, with the largest shift occurring in the northern two regions
200 (Oregon/Northern California and Washington; Figure 3 and S1). Generally, ARs that make landfall
201 further north on the U.S. West Coast tend to have genesis further west, with over 25° longitude
202 difference between the median AR genesis centroid location for Washington compared to the
203 Oregon/Northern California region. The median longitude of AR genesis shifts between 8° and 27°
204 westward when considering the most damaging ARs (90th percentile of damage) compared to all ARs.
205 The median landfalling AR IVT also increases with damage percentile level; ARs that cause damage in
206 the 90th percentile have a median landfalling IVT 224 to 369 kg m⁻¹ s⁻¹ greater than the median
207 landfalling IVT of the full AR dataset (increases of 57% to 82%).

208 Corringham et al. (2019) quantified the relationship between financial cost and AR IVT, demonstrating
209 that higher IVT is associated with increasing damages in a near exponential relationship (validated here
210 in Figure S2). The results presented here are in agreement, with higher IVT providing a suitable
211 explanation for why these ARs are more damaging, with many studies identifying the intrinsic
212 relationship between AR IVT and precipitation/flooding (Neiman et al., 2009; Konrad and Dettinger
213 2017; Ralph et al., 2019). ARs from the Western Pacific tend to have a higher IVT and persist for longer
214 compared to Eastern Pacific ARs (Zhou et al., 2018; Zhou and Kim 2019). Payne and Magnusdottir
215 (2014) discussed that the enhanced zonal winds that allow for propagation of ARs from further across

216 the Pacific may be the reason why these ARs tend to also have elevated moisture fluxes. Scavenging of
217 water vapor along the AR track may also occur, as moisture from previous cyclonic and frontal systems
218 may converge and intensify a migrating AR (Sodemann and Stohl, 2013; Sodemann et al., 2020).
219 Crucially, the results presented here demonstrate that AR landfalling IVT tends to increase with genesis
220 distance from landfall, regardless of the location within the Pacific Ocean. There is not a particular
221 location where damaging ARs have genesis, but rather, damaging ARs have genesis further from
222 landfall compared to the distribution of all ARs that make landfall for each region.

223 *3.2 Atmospheric conditions at genesis*

224 The position of the AR genesis low pressure anomaly appears as the dominant driver for controlling the
225 location of landfall (Figure 4a, S3). Zhang et al. (2019) found that about 82% of ARs are associated
226 with extratropical cyclones (ECs) and while ECs are not objectively identified in this study, the
227 composite atmospheric conditions during AR genesis certainly indicate that AR genesis is generally
228 associated with EC activity. For Washington, the low pressure anomaly is centred in the Gulf of Alaska
229 with the centre of the anomaly shifting southeast for each region southward down the U.S West Coast.
230 The position of the genesis low pressure anomaly close to the coastline appears similar to previously
231 presented landfalling anomalies for each location (Guirguis et al., 2018), which may be attributed to the
232 majority of ARs that have genesis locations reasonably close to the coastline (Figure 2). Another point
233 of interest regarding the position of all AR genesis is the increasing size and magnitude of the high
234 pressure anomaly on the northwest side of the low pressure anomaly (in the Gulf of Alaska) for ARs
235 making landfall further south, suggesting that ridging may be more persistent during genesis of ARs
236 that landfall on the southern U.S. West Coast. The IVT vector anomaly demonstrates the broad elevated
237 geostrophic flow directed towards the coastline on the south/southeast edge of the low pressure
238 anomaly. In California and Baja California there is also a substantial counterflow anomaly on the
239 northwest edge of the low pressure associated with the more established dipole pressure anomaly. The
240 elevated IVT vector anomalies are also colocated with elevated 300hPa zonal wind anomalies.

241 When considering the subset of damaging ARs (75th percentile) the magnitude of the pressure anomalies
242 become greater along with larger regions of elevated IVT extending further westward across the Pacific
243 (Figure 4a). The magnitude of the 300hPa zonal wind anomaly is also greater for these damaging ARs
244 and generally covers a larger area, most notably for Oregon/Northern California where the zonal wind
245 anomaly extends zonally across the entire north Pacific basin. The high pressure anomalies are also
246 more prevalent for damaging ARs. Lower EC pressures have been previously associated with AR IVT
247 intensity (e.g. Zhang et al., 2019) and the results presented here directly links the magnitude of the low
248 pressure anomaly at AR genesis to increased economic impact following landfall.

249 Figure 4b presents the same atmospheric composites and anomalies as Figure 4a, but for the subset of
250 ARs with genesis locations in the western region of the north Pacific basin as defined by Zhou and Kim
251 (2019, westward of 170°W). The pressure anomalies are much larger than Figure 4a with a broad
252 zonally extended low pressure region spanning the north Pacific basin, possibly exhibiting the
253 progression of multiple ECs, particularly for the most damaging ARs in Oregon/Northern California
254 that originate from the Western Pacific. This suggestive waveguide is similar to those presented by Fish
255 et al. (2019) when identifying AR families; ARs making landfall in rapid succession. Cordeira et al.
256 (2013) provides an example of an AR that caused flooding in the Western U.S. which originates off the
257 coast of Japan, demonstrating that multiple cyclonic systems may be associated with the progression of
258 a single AR from the Western Pacific (discussed further in Sodemann et al., 2020). The elevated IVT
259 extending throughout the entire Pacific also suggests that at the point of AR genesis in the western
260 Pacific, there are elevated moisture fluxes downstream (possible concurrent ARs) already making
261 landfall on the U.S. West Coast. The zonally extended 300hPa jet stream (with a maximum zonal core
262 at 35°N) observed in Figure 4b is also congruent with findings from Cordeira et al. (2013), Payne and
263 Magnúsdóttir (2014) and Fish et al. (2019), allowing for the zonal propagation of ECs and associated
264 ARs across the entire Pacific, also suggesting that the occurrence of damaging ARs from the West
265 Pacific may be associated with the rapid progression of multiple ARs (i.e. an AR family).

2664. **Conclusions**

267 ARs account for 88% of annual total flood damages in the Western U.S., causing on average \$1.1 billion
268 of damage annually. Presented here is the initial examination linking AR flood damage to atmospheric
269 dynamics through a study of AR genesis. ARs that cause substantial economic impact to the Western
270 U.S. are unique in both their lifecycle and magnitude, with the most impactful events tending to
271 originate from further across the ocean prior to landfall paired with a substantially higher moisture flux
272 at landfall. ARs that cause extreme damage (90th percentile) tend to have genesis locations between 8°
273 and 27° longitude further westward and IVT increases of 57% to 82% compared to all ARs that make
274 landfall on the U.S. West Coast. The relationship found between AR impacts and genesis location will
275 help inform targeted deployment of future observation campaigns (AR Recon). Due to the relative
276 importance of West Pacific ARs, there may be a possibility to improve longer lead forecasts of extreme
277 precipitation by observing ARs at genesis in these westward locations, a region not currently considered
278 for AR Recon. Linking AR dynamics and lifecycle to economic impact also provides an opportunity to
279 explore impact-based AR forecasting along with facilitating the study of how changing atmospheric
280 dynamics in the Pacific Ocean may influence flood damages experienced in the Western U.S.

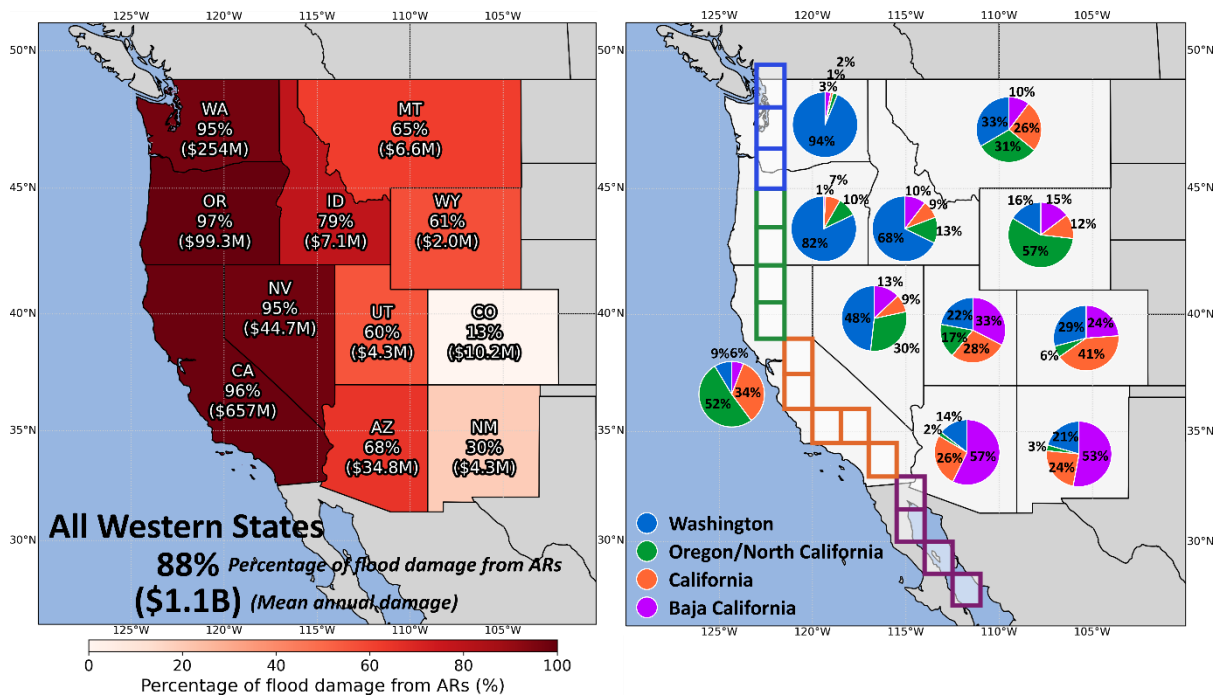
281 **Data availability statement**

282 The AR data are available at <https://ucla.box.com/ARcatalog>. Development of the AR detection
283 algorithm and databases was supported by NASA. AR detection is based on the algorithm originally
284 introduced in Guan and Waliser (2015), refined in Guan et al. (2018), and further enhanced in Guan
285 and Waliser (2019) with tracking capability. Flood damages in the Western U.S. were retrieved through
286 the National Flood Insurance Program retrieved from the U.S. Federal Emergency Management
287 Agency, downloaded 2019-10-25 ([https://www.fema.gov/openfema-data-page/fima-nfip-redacted-
288 claims-v1](https://www.fema.gov/openfema-data-page/fima-nfip-redacted-claims-v1)).

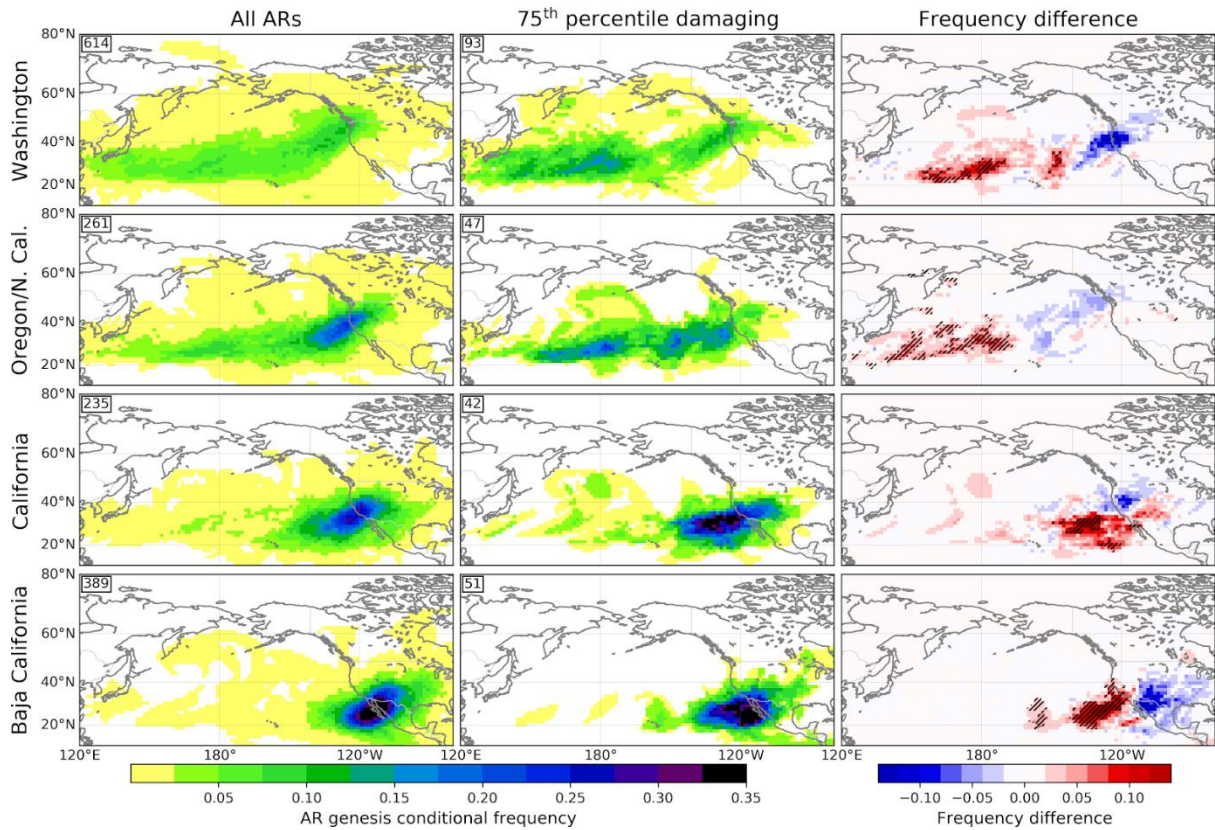
- 290 Corringham, T. W., Ralph, F. M., Gershunov, A., Cayan, D. R. and Talbot, C. A. (2019). Atmospheric
291 rivers drive flood damages in the western United States. *Science Advances*, 5(12), 1-7.
292 <https://doi.org/10.1126/sciadv.aax4631>
- 293 Dee, D. P., Uppala, S. M., Simmons, A. J., Berrisford, P., Poli, P., Kobayashi, S., et al. (2011). The
294 ERA-Interim reanalysis: Configuration and performance of the data assimilation system.
295 *Quarterly Journal of the Royal Meteorological Society*, 137(656), 553–597.
296 <https://doi.org/10.1002/qj.828>
- 297 Dettinger, M. D., Ralph, F. M., Das, T., Neiman, P. J. and Cayan, D. R. (2011). Atmospheric rivers,
298 floods and the water resources of California. *Water*, 3, 445–478.
299 <https://doi.org/10.3390/w3020445>
- 300 Eiras-Barca, J., Ramos, A. M., Algarra, I., Vázquez, M., Dominguez, F., Miguez-Macho, G., et al.
301 (2021). European West Coast atmospheric rivers: A scale to characterize strength and impacts.
302 *Weather and Climate Extremes*, 31, p.100305. <https://doi.org/10.1016/j.wace.2021.100305>
- 303 Fish, M. A., Wilson, A. M. and Ralph, F. M. (2019). Atmospheric river families: Definition and
304 associated synoptic conditions. *Journal of Hydrometeorology*, 20(10), 2091-2108.
305 <https://doi.org/10.1175/JHM-D-18-0217.1>
- 306 Guan, B. and Waliser, D. E. (2015). Detection of atmospheric rivers: Evaluation and application of an
307 algorithm for global studies. *Journal of Geophysical Research: Atmospheres*, 120, 12,514-
308 12,535. <https://doi.org/10.1002/2015JD024257>
- 309 Guan, B. and Waliser, D. E. (2017). Atmospheric rivers in 20 year weather and climate simulations: A
310 multimodel, global evaluation, *Journal of Geophysical Research: Atmospheres*, 122, 5556–
311 5581, <https://doi.org/10.1002/2016JD026174>
- 312 Guan, B. and Waliser, D. E. (2019). Tracking Atmospheric Rivers Globally: Spatial Distributions and
313 Temporal Evolution of Life Cycle Characteristics. *Journal of Geophysical Research:
314 Atmospheres*, 124, <https://doi.org/10.1029/2019JD031205>
- 315 Guan, B., Waliser, D. E. and Ralph, F. M. (2018). An intercomparison between reanalysis and
316 dropsonde observations of the total water vapor transport in individual atmospheric rivers.
317 *Journal of Hydrometeorology*, 19(2), 321-337. <https://doi.org/10.1175/JHM-D-17-0114.1>
- 318 Guirguis, K., Gershunov, A., Clemesha, R. E. S., Shulgina, T., Subramanian, A. C., and Ralph, F. M.
319 (2018). Circulation drivers of atmospheric rivers at the North American West Coast.
320 *Geophysical Research Letters*, 45, 12,576–12,584. <https://doi.org/10.1029/2018GL079249>
- 321 Konrad, C. P. and Dettinger, M. D. (2017). Flood runoff in relation to water vapor transport by
322 atmospheric rivers over the western United States, 1949–2015. *Geophysical Research Letters*,
323 44, 11,456–11,462. <https://doi.org/10.1002/2017GL075399>
- 324 Neiman, P. J., Ralph, F. M., Moore, B. J., Hughes, M., Mahoney, K. M., Cordiera, J. M. and Dettinger,
325 M. D. (2013). The landfall and inland penetration of a flood-producing atmospheric river in
326 Arizona. Part I: Observed synoptic-scale, orographic, and hydrometeorological characteristics.
327 *Journal of Hydrometeorology*, 14(2), 460-484. <https://doi.org/10.1175/JHM-D-12-0101.1>
- 328 Neiman, P. J., Ralph, F. M., Wick, G. A., Lundquist, J. D. and Dettinger, M. D. (2008). Meteorological
329 characteristics and overland precipitation impacts of atmospheric rivers affecting the West
330 Coast of North America based on eight years of SSM/I satellite observations. *Journal of
331 Hydrometeorology*, 9, 22-47. <https://doi.org/10.1175/2007JHM855.1>
- 332 Neiman, P. J., White, A. B., Ralph, F. M., Gattas, D. J. and Gutman, S. I. (2009). A water vapour flux
333 tool for precipitation forecasting. *Proceedings of the Institution of Civil Engineers Water
334 Management* (162, WM2). 83–94. <https://doi.org/10.1680/wama.2009.162.2.83>
- 335 O'Brian, T., Payne, A. E., Shields, C. A., Rutz, J., Brands, S., Castellano, C. et al. (2020). Detection
336 uncertainty matters for understanding atmospheric rivers. *Bulletin of the American
337 Meteorological Society, Meeting Summary*, E790–E796. <https://doi.org/10.1175/BAMS-D-19-0348.1>
- 339 Paltan, H., Waliser, D., Lim, W. H., Guan, B., Yamazaki, D., Pant, R., and Dadson, S. (2017). Global
340 floods and water availability driven by atmospheric rivers. *Geophysical Research Letters*, 44,
341 10,387–10,395. <https://doi.org/10.1002/2017GL074882>

- 342 Payne, A. E. and Magnusdottir, G. (2014). Dynamics of Landfalling Atmospheric Rivers over the North
343 Pacific in 30 Years of MERRA Reanalysis. *Journal of Climate*, 27(18), 7133-7150.
344 <https://doi.org/10.1175/JCLI-D-14-00034.1>
- 345 Prince, H. D., Cullen, N. J., Gibson, P. B., Conway, J. and Kingston, D. G. (2021). A climatology of
346 atmospheric rivers in New Zealand. *Journal of Climate*, Early Online Release, 1-56.
347 <https://doi.org/10.1175/JCLI-D-20-0664.1>
- 348 Ralph, F. M., Rutz, J. J., Cordeira, J. M., Dettinger, M., Anderson, M., Reynolds, D., Schick, L. J. and
349 Smallcomb, C. (2019). A scale to characterize the strength and impacts of atmospheric rivers.
350 *Bulletin of the American Meteorological Society*, 100(2), 269-289.
351 <https://doi.org/10.1175/BAMS-D-18-0023.1>
- 352 Rutz, J. J., and Steenburgh, W. J. (2012). Quantifying the role of atmospheric rivers in the interior
353 western United States. *Atmospheric Science Letters*, 13, 257-261,
354 <https://doi.org/10.1002/asl.392>
- 355 Rutz, J. J., Guan, B., Bozkurt, D., Valenzuela, R., Gorodetskaya, I. V., Gershunov, A. et al. (2020).
356 'Global and Regional Perspectives', Ralph, F. M. (eds), *Atmospheric Rivers*, Springer Nature,
357 Switzerland, 89-140. https://doi.org/10.1007/978-3-030-28906-5_4
- 358 Rutz, J. J., Shields, C. A., Lora, J. M., Payne, A. E., Guan, B., Ullrich, P. et al. (2019), The Atmospheric
359 River Tracking Method Intercomparison Project (ARTMIP): Quantifying uncertainties in
360 atmospheric river climatology, *Journal of Geophysical Research: Atmospheres*, 124, 13777-
361 13802, <https://doi.org/10.1029/2019JD030936>
- 362 Schreck, C. J. III, Knapp, K. R. and Kossin, J. P. (2014). The impact of best track discrepancies on
363 global tropical cyclone climatologies using IBTrACS. *Monthly Weather Review*, 142(10),
364 3881-3899. <https://doi.org/10.1175/MWR-D-14-00021.1>
- 365 Shearer, E. J., Nguyen, P., Sellars, S. L., Analui, B., Kawzenuk, B., Hsu, K., et al.
366 (2020). Examination of global midlatitude atmospheric river lifecycles using an object-
367 oriented methodology. *Journal of Geophysical Research: Atmospheres*, 125,
368 e2020JD033425. <https://doi.org/10.1029/2020JD033425>
- 369 Shields, C. A., Rutz, J. J., Leung, L.-Y., Ralph, F. M., Wehner, M., Kawzenuk, B. et al. (2018).
370 Atmospheric River Tracking Method Intercomparison Project (ARTMIP): Project goals and
371 experimental design. *Geoscientific Model Development*, 11, 2455-2474.
372 <https://doi.org/10.5194/gmd-11-2455-2018>
- 373 Sodemann, H., and Stohl, A. (2013). Moisture origin and meridional transport in atmospheric rivers and
374 their association with multiple cyclones. *Monthly Weather Review*, 141, 2850-2868.
375 <https://doi.org/10.1175/MWR-D-12-00256.1>
- 376 Sodemann, H., Wernli, H., Knippertz, P., Cordeira, J. M., Dominguez, F., Guan, B. et al. (2020).
377 'Structure, Process and Mechanism', Ralph, F. M. (eds), *Atmospheric Rivers*, Springer Nature,
378 Switzerland, 15-43. https://doi.org/10.1007/978-3-030-28906-5_2
- 379 Vano, J. A., Miller, K., Dettinger, M. D., Cifelli, R., Curtis, D., Dufour, A., Olsen, J. R. and Wilson, A.
380 M. (2019). Hydroclimatic extremes as challenges for the water management community:
381 Lessons from Oroville Dam and hurricane Harvey. *Bulletin of the American Meteorological*
382 *Society*, 100, S9-S14. <https://doi.org/10.1175/BAMS-D-18-0219.1>
- 383 Waliser, D. and Guan, B. (2017). Extreme winds and precipitation during landfall of atmospheric rivers.
384 *Nature Geoscience*, 10, 179-183 <https://doi.org/10.1038/NGEO2894>
- 385 White, A. B., Moore, B. J., Gottas, D. J., Neiman P. J. (2019). Winter storm conditions leading to
386 excessive runoff above California's Oroville Dam during January and February 2017. *Bulletin*
387 *of the American Meteorological Society*, 100, 55-70. <https://doi.org/10.1175/BAMS-D-18-0091.1>
- 389 Zhang, Z., Ralph, F. M., and Zheng, M. (2019). The relationship between extratropical cyclone strength
390 and atmospheric river intensity and position. *Geophysical Research Letters*, 46, 1814-1823.
391 <https://doi.org/10.1029/2018GL079071>
- 392 Zhou, Y., and Kim, H. (2019). Impact of Distinct Origin Locations on the Life Cycles of Landfalling
393 Atmospheric Rivers Over the U.S. West Coast. *Journal of Geophysical Research:*
394 *Atmospheres*, 124, 11,897-11,909. <https://doi.org/10.1029/2019JD031218>

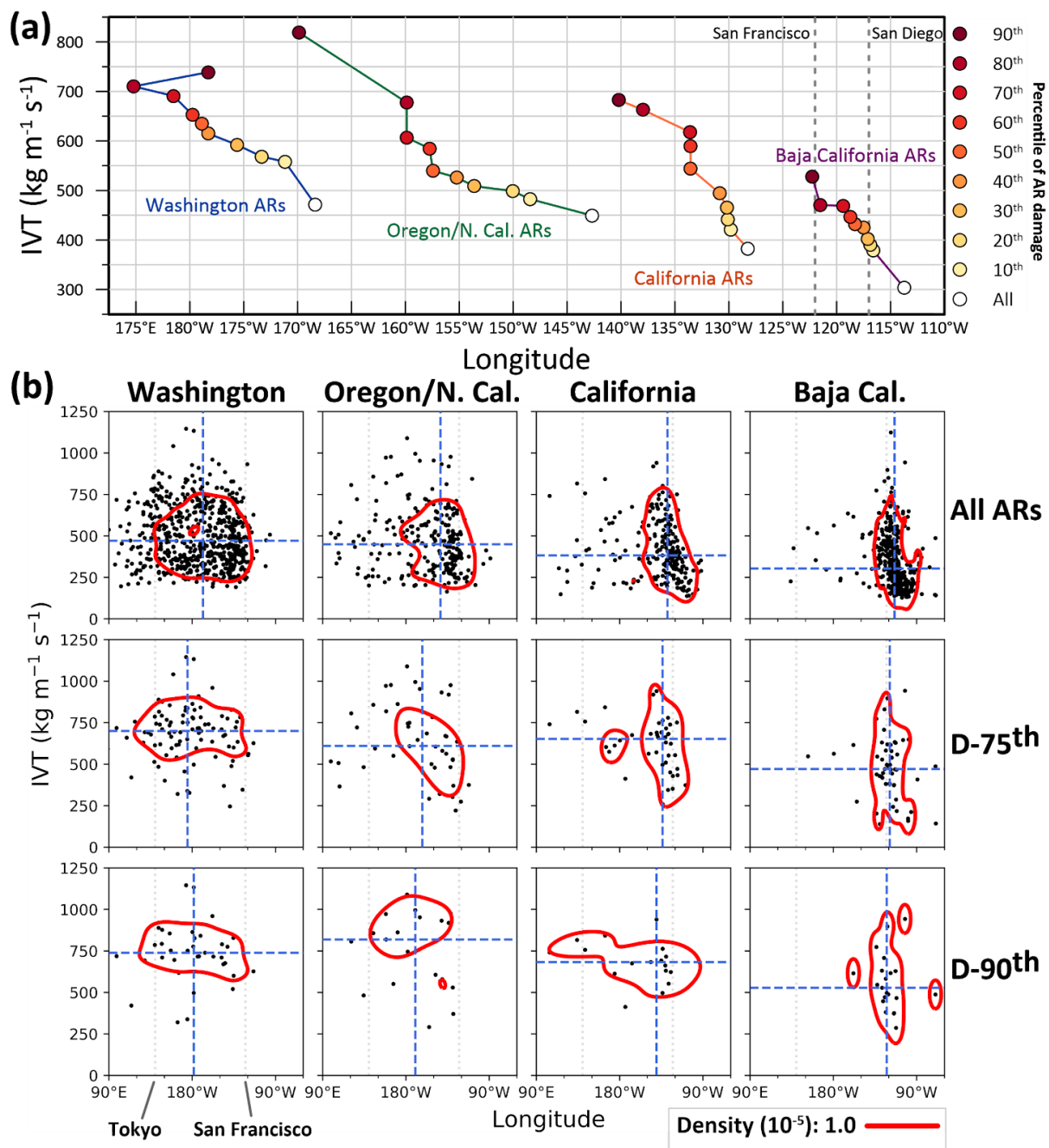
- 395 Zhou, Y., Kim, H., and Guan, B. (2018). Life cycle of atmospheric rivers: Identification and
396 climatological characteristics. *Journal of Geophysical Research: Atmospheres*, 123, 12,715–
397 12,725. <https://doi.org/10.1029/2018JD029180>
- 398 Zhu, Y. and Newell, R. E. (1994). Atmospheric rivers and bombs. *Geophysical Research Letters*,
399 21(18), 1999-2002. <https://doi.org/10.1029/94GL01710>



400 **Figure 1.** (left) The percentage of mean annual flood damage in the Western continental U.S. by state, caused by
 401 ARs with the resulting mean annual cost of ARs shown in parentheses. (right) The coastline of the Western U.S.
 402 is divided into four broad regions (Washington - blue, Oregon/North California - green, California - orange and
 403 Baja California - purple) to study the genesis locations of ARs that make landfall in different locations. The
 404 proportion of damage in each state caused by landfalling ARs from each portion of coastline is shown in the pie
 405 charts.



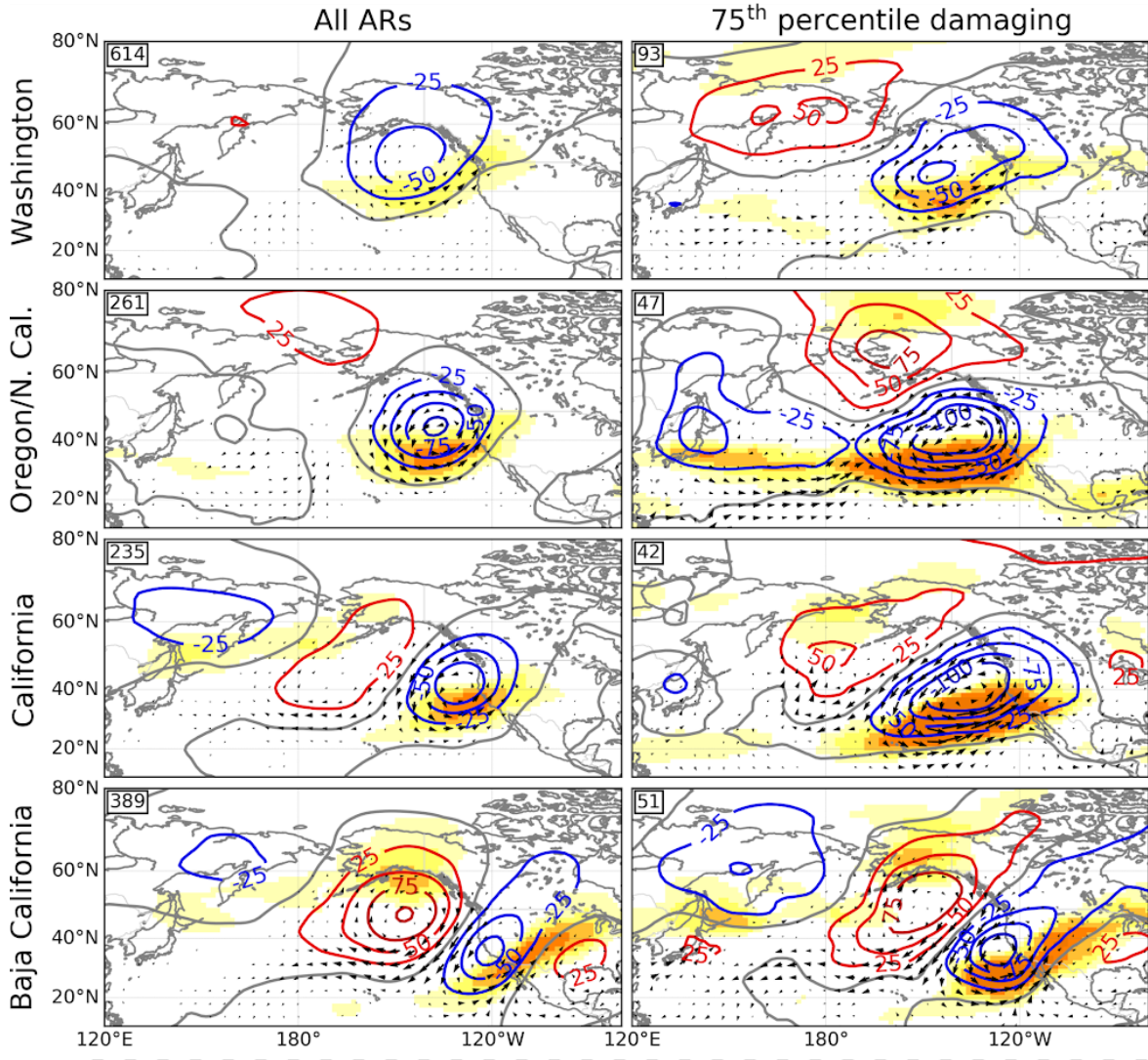
406 **Figure 2.** Conditional frequency of AR genesis for ARs making landfall in the four regions defined in Figure 1
 407 for all landfalling ARs (left) and those that produce damage in the 75th percentile (centre). Conditional frequency
 408 is the probability an AR object originates from a grid cell given that it makes landfall in each location and causes
 409 damage in the specified range (i.e. exceeding the 75th percentile). The numerical absolute increase in frequency is
 410 shown (right) with statistical significance ($p < 0.1$) shown with dashed lines (from a one-sided Fisher-exact test).



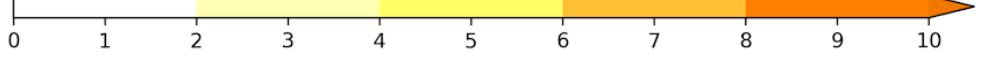
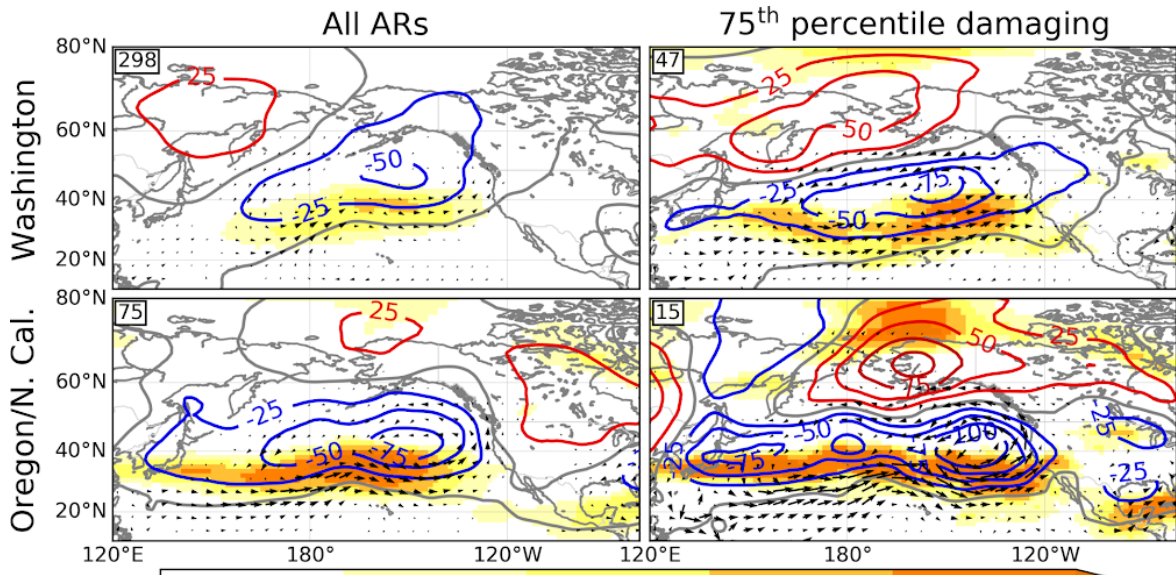
411

412 **Figure 3.** (a) Median AR genesis longitude and landfalling IVT for different damage percentiles for each region.
 413 Data points coloured for each percentile level, white to red, with white dots representing the full AR database both
 414 damaging and non-damaging. The longitude of San Francisco and San Diego are shown with the grey dotted lines
 415 to give context of the U.S. West Coast. (b) The distribution of AR genesis longitude and landfalling IVT for all
 416 ARs, ARs that cause damage in the 75th percentile (D-75th) and ARs that cause damage in the 90th percentile (D-
 417 90th). Density shown in red as calculated with KDE (gaussian filter and Scott's bandwidth). The median of each
 418 distribution is shown with the blue dotted lines and the location of Tokyo and San Francisco shown with light
 419 grey dotted lines to provide context of the North Pacific basin.

Full AR dataset



West Pacific AR subset



300 hPa zonal wind anomaly (m s^{-1})

\rightarrow = $200 \text{ kg m}^{-1} \text{ s}^{-1}$

421 **Figure 4.** Atmospheric conditions at the time of AR genesis shown with composites of anomalous 6-hourly Z500
422 (red/blue 25 m contours for positive/negative anomalies, zero line shown in grey), 300hPa zonal wind anomaly
423 (orange shading) and IVT vector anomaly (vector magnitude greater than $15 \text{ kg m}^{-1}\text{s}^{-1}$). Composites at the time of
424 genesis are shown for (left) all landfalling ARs and (right) ARs that produce damage in the 75th percentile. The
425 number of AR genesis events considered for each plot is shown in the top left corner. A subset of ARs with genesis
426 locations in the Northwest Pacific Ocean (west of 170°W) are shown for Oregon/N. Cal. And Washington in the
427 lower plot.

1
2
3
4
5
6
7
8
9
10
11

Supplementary material for

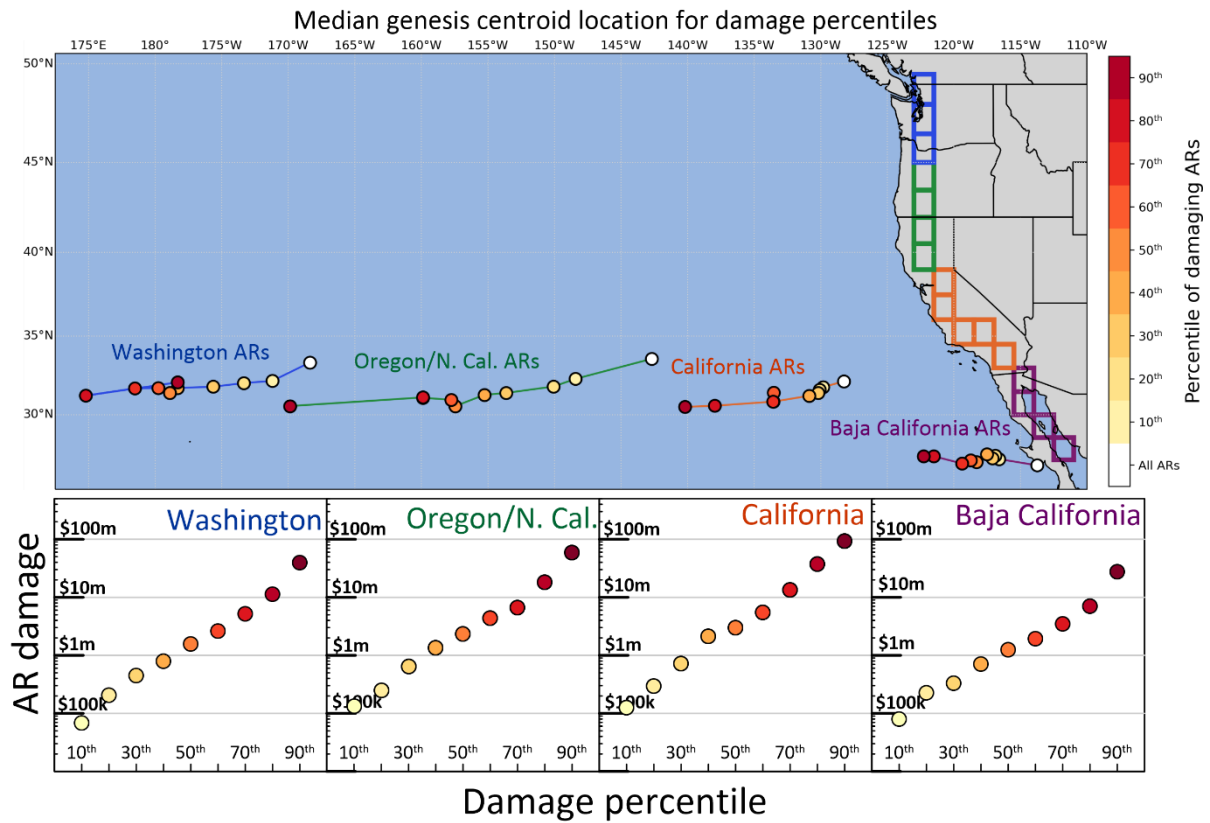
**Genesis locations of the costliest atmospheric rivers impacting the western
United States**

**Hamish D. Prince^{*}, Peter B. Gibson, Michael J. DeFlorio, Thomas W, Corringham,
Alison Cobb, Bin Guan, F. Martin Ralph and Duane E. Waliser**

**Corresponding author:* Hamish Prince, prince.hamishd@gmail.com

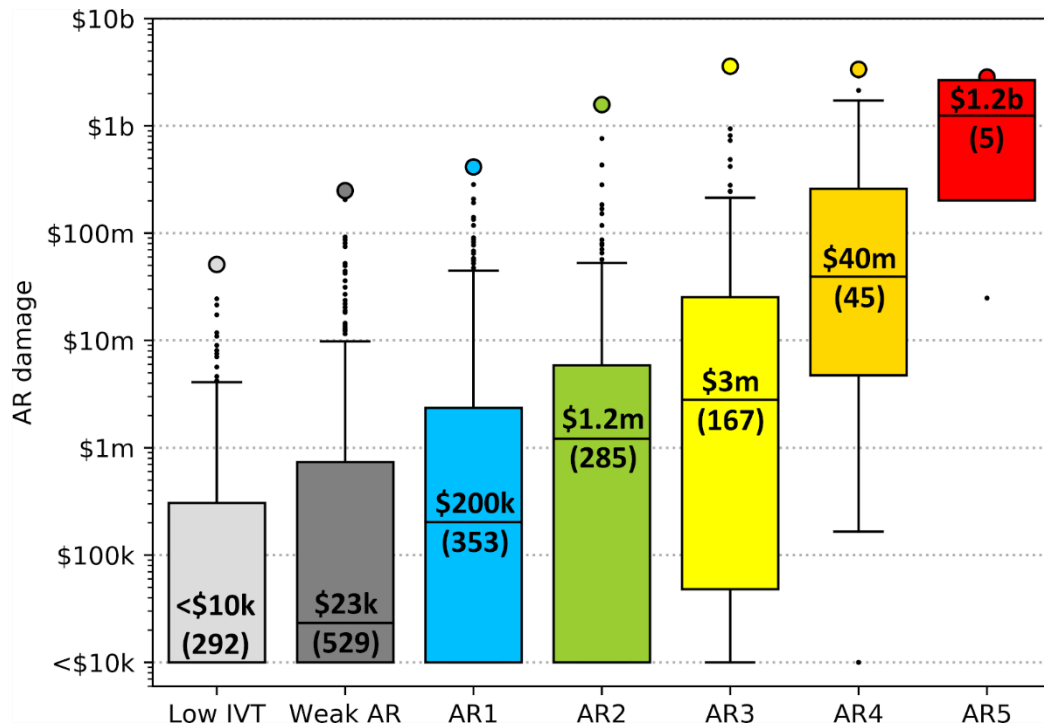
The document includes:

- Supplementary Figure S1. Median genesis centroid locations
- Supplementary Figure S2. Ranked AR damages on U.S. West Coast
- Supplementary Figure S3. Schematic of damaging AR genesis objects and associated atmospheric conditions

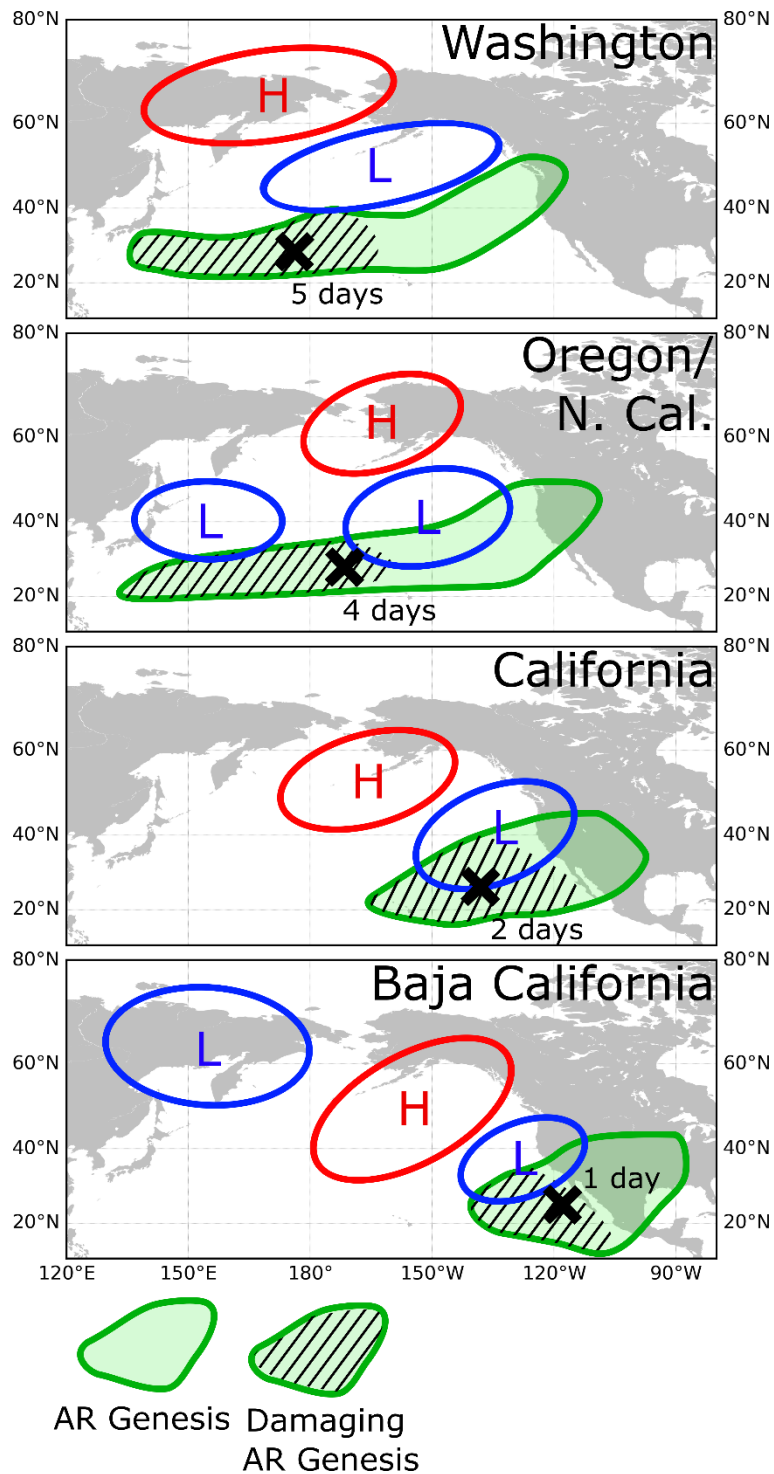


12

13 **Supplementary Figure 1.** (upper) The median genesis centroid location of ARs that cause damage in the Western
 14 U.S. for different damage percentiles (coloured white to red, white representing all ARs that make landfall).
 15 (lower) The median damage associated with each percentile level for the four regions.



16 **Supplementary Figure 2.** Winter (NDJFM) flood damages associated with ARs detected by GW_{19} and ranked
 17 with the Ralph et al. (2019) AR scale. Median damages and number (in parentheses) of ARs displayed for each
 18 rank, boxes are 25th and 75th percentiles, whiskers are 5th and 95th percentiles and colored dots are maximums.
 19 The Low IVT rank (detected ARs with IVT less than $250 \text{ kg m}^{-1}\text{s}^{-1}$) as proposed by Prince et al. (2021) is used to
 20 facilitate full cohesion between AR detection (Guan and Waliser, 2019) and ranking (Ralph et al., 2019).



22 **Supplementary Figure 3.** Schematic of AR genesis locations and atmospheric conditions associated with genesis
 23 for ARs impacting the U.S. West Coast for ARs making landfall in the four regions defined in Figure 1. AR
 24 genesis footprint shown with green shading, representing the full range of AR object outlines at the point of
 25 genesis. The full range of damaging (exceeding 75th percentile) AR genesis object outlines are shown with black
 26 hatching over the green shading. The pressure anomalies typically associated with the genesis of these damaging
 27 ARs are shown with the red (high pressure) and blue (low pressure) contours. Median AR centroid location for
 28 damaging ARs shown with black crosses paired with the median number of days between genesis and the day of
 29 maximum landfalling IVT.